Catalysis Science & Technology

ROYAL SOCIETY OF CHEMISTRY

PAPER

View Article Online
View Journal | View Issue

Cite this: *Catal. Sci. Technol.*, 2025, 15, 4002

Regulating protonation paths for enhanced photocatalytic CO_2 methanation by coupling Pt sites on $WO_{2.9}/TiO_2$†

Jiajun Du,[a] Jun Deng,[a] ChangAn Zhou,[a] Hairong Yue,[a] Chong Liu,[a] Patrik Schmuki,[b] Štěpán Kment[c] and Xuemei Zhou *[a]

Received 12th February 2025,
Accepted 21st May 2025

DOI: 10.1039/d5cy00167f

rsc.li/catalysis

CO_2 methanation *via* photocatalysis with water vapor is a sustainable technique for reducing CO_2 emission but is challenged by the high energy barrier associated with the initial adsorption, activation and protonation of CO_2 molecules. In this work, a substoichiometric $WO_{2.9}$ thin film with strong Lewis acidity was coated on TiO_2 microspheres, followed by the deposition of Pt cocatalysts on $WO_{2.9}$ with controlled Pt single atoms and clusters (Pt–$WO_{2.9}/TiO_2$). The methane production rate reached 10.74 μmol h^{-1} g^{-1} with a selectivity of 99.8%, which was ~40 times higher than that of bare TiO_2 (0.27 μmol h^{-1} g^{-1}). The high methane production rate was attributed to the synergy of Pt sites on the $WO_{2.9}/TiO_2$ heterojunction, where the Pt clusters facilitated water dissociation, thereby providing H* through hydrogen spillover on the surface, and the presence of a substoichiometric $WO_{2.9}$ surface further enhanced the spillover process. The high density of active H* promoted the protonation pathway for CO_2 activation (CO_2 → $COOH^+$ → *COOH), which improved the adsorption of the essential intermediate *CO on Pt single atoms and displayed a significantly reduced energy barrier for the protonation reaction of C1 intermediates, resulting in a mixed reaction pathway. This work provides new insights into a mechanism to regulate the reaction path to facilitate efficient photocatalytic CO_2 methanation.

1. Introduction

Methane is the main component of natural gas and is widely used as a clean energy source or raw material for bulk production of chemicals.[1] In industry, CH_4 is synthesized using CO_2 and H_2 as raw materials *via* the Sabatier reaction,[2] but the carbon emission and energy consumption of the process need to be improved. With the increasing demand for natural gas in the coming decades,[3] CH_4 synthesis *via* a green and sustainable approach is highly promising, with photocatalysis emerging as a method to achieve CO_2 methanation from solar energy. However, owing to the high thermodynamical stability of CO_2, it is challenging to achieve high methane yield *via* photocatalysis.[4] Moreover, the conversion from CO_2 to CH_4 is an eight-electron reduction reaction that requires a high density of protons and electrons, resulting in relatively slow reaction kinetics.[5] In addition, the competing reaction for CO_2 reduction is the recombination of protons to form hydrogen. Therefore, photocatalysts that can accumulate photogenerated electrons and promote the migration of protons to carbon intermediates may enhance methane production.[6]

The substoichiometric tungsten oxides, such as $WO_{2.72}$, $W_{24}O_{68}$ and $WO_{2.9}$, are stable in air,[7] and the light absorption of WO_{3-x} can be extended to the near-infrared region owing to the defect states below the conduction band minimum (CBM).[8,9] The V_O (oxygen vacancy) and unsaturated metal coordination sites pair can be used as Lewis acid sites to adsorb and activate CO_2 molecules by reducing the activation energy barrier of CO_2 molecules.[10] In addition, W(VI) sites in WO_{3-x} can be used as electron reservoirs by reducing them to W(V).[11] The tungsten oxide with oxygen deficiency (V_O) as substoichiometric tungsten oxides (WO_{3-x}) are introduced to construct a heterojunction with TiO_2 to improve the charge transfer kinetics of titania and increase the electron density on the surface. Titania is the most investigated semiconductor in photocatalysis due to its high abundance, high chemical stability and resistivity, but it is limited by its overall low reaction rate. In this work, mesoporous TiO_2 microspheres were used as a support for substoichiometric

[a] *School of Chemical Engineering, Sichuan University, No. 24 South Section 1, Yihuan Road, Chengdu, 610065, People's Republic of China. E-mail: xuemeizhou@scu.edu.cn*
[b] *Department of Materials Science and Engineering, Friedrich-Alexander-University Erlangen-Nurnberg, Martensstraße 7, 91058 Erlangen, Germany*
[c] *Regional Centre of Advanced Technologies and Materials, Czech Advanced Technology and Research Institute, Palacký University, Křížkovského 511/8, 779 00 Olomouc, Czech Republic*

† Electronic supplementary information (ESI) available. See DOI: https://doi.org/10.1039/d5cy00167f

tungsten oxide loading. The mesoporous structure and high surface area can provide abundant exposed active sites for surface reduction reactions and facilitate the construction of heterojunctions with intimate interfacial contact. The closely contacted anatase/rutile phase junctions, combined with highly crystalline anatase and rutile nanoparticles, may synergistically promote charge separation and transport.[12,13]

For methane production, noble metal cocatalysts can effectively enhance photocatalytic activity because of their electron transfer ability.[14–16] However, hydrogen evolution reaction, which is a competing reaction in CO_2 reduction, can also be accelerated by noble metals as well.[17] Previous studies have shown that the coordination environment,[16,18] size and distribution[19] of Pt can effectively inhibit hydrogen evolution. It was reported in the 1960s that hydrogen spillover from noble metals to the oxide support occurred at the interface between the metal and the support.[20] For example, it has recently been demonstrated that Pt nanoparticles (Pt NPs) dissociate H_2O into absorbed H atoms (*H) and spillover from Pt NPs to the CO_2 adsorption sites on the support to produce methane.[16]

Moreover, the activation of CO_2 during photoreduction involves two different pathways: activation by electrons ($CO_2 \rightarrow \cdot CO_2^-$) and protonation ($CO_2 \rightarrow COOH^+$). Recently, experiments have demonstrated that CO_2 activation *via* protonation on semiconductor photocatalysts, forming an $O{=}C{=}O{-}H^+$ intermediate,[21] can significantly decrease the reaction energy barrier when such an intermediate undergoes further multiple proton-electron coupling reactions. Therefore, it is essential to design photocatalysts that favor the protonation of CO_2. In this work, substoichiometric $WO_{2.9}$ was fabricated on TiO_2 microspheres for photocatalytic CO_2 methanation, where the deposition of Pt cocatalysts and substoichiometric $WO_{2.9}$ with good distribution can be expected to control the hydrogen spillover and improve the methane production rate (Scheme 1).

2. Experimental

2.1 Chemicals and materials

Pluronic F127 ($(H(OC_2H_4)_x(OC_3H_3)_y(O_2H_4)_zOH$, M_w = 15 000 g mol^{-1}), $H_2PtCl_6{\cdot}6H_2O$, WCl_6 (99.9%), tetrahydrofuran (THF, 99.9%), sodium bicarbonate (99%) and tetrabutyltitanate (TBOT, 99%) were purchased from Adamas. Acetic acid (AcOH, 99%), absolute ethyl alcohol (C_2H_5OH, 99.8%), and hydrochloric acid (HCl, 37 wt%) were purchased from *Chron* in Chengdu. Ultrapure water (resistivity: 17.38 MΩ cm) was used in the synthetic process. All reagents were used as received without further purification.

2.2 Synthesis of the catalysts

Synthesis of TiO_2 microspheres. In a typical procedure, 1 mL of HOAc and HCl (37 wt%) was dropped in 15 mL of THF. 0.75 g F127 yellow powder was slowly introduced into the above solution. The mixture was vigorously stirred to form a clear and transparent solution. Subsequently, 1.7 mL of TBOT was dropped under vigorous stirring to form a clear yellow solution. The yellow solution was then left in a drying oven to evaporate the THF solvents at 40 °C for 20 h and at 80 °C for another 10 h. The obtained precipitate was calcined in a tubular furnace under N_2 flow at 400 °C for 3 h. Finally, the white powder was obtained by calcination in a muffle furnace at 400 °C for 3 h.

Synthesis of $WO_{2.9}/TiO_2$ microspheres. In the N_2 atmosphere, 17.1 mg WCl_6 and 100 mg TiO_2 microspheres were dispersed and dissolved in 40 mL of anhydrous ethanol, and the mixture was continuously stirred for 3 hours in an ice-water bath. After that, it was poured into a 50 mL hydrothermal kettle and kept in an oven at 180 °C for 12 hours. After natural cooling to room temperature, the samples were washed three times with deionized water, dried in a vacuum oven at 60 °C, and calcined at 400 °C in a 5% Ar/H_2 atmosphere for 2 hours.

Synthesis of Pt–$WO_{2.9}/TiO_2$ microspheres. 100 mg $WO_{2.9}/TiO_2$ microspheres were dispersed in 20 mL DI water, 1 mg chloroplatinic acid was added and sonicated in N_2 atmosphere and ice water bath for 40 minutes. After freezing in the refrigerator (−20 °C) for 16 hours, keep it frozen and irradiate it with 275 nm ultraviolet light for 1 h in an ice/water bath. After the natural melting of the ice and the temperature reaching room temperature, the powders were centrifuged, washed three times with DI water and dried overnight at 80 °C in a vacuum oven.

2.3 Material characterization

The morphology of all samples was observed on a field emission scanning electron microscope (FESEM) (JEOL, JSM-7500, Japan). Transmission electron microscope (TEM) images were acquired with a Japan JEOL-F200 at an acceleration voltage of 200 kV. Samples were dispersed in ethanol, and 10 μL suspension was dropped on an ultra-thin carbon film supported by a 300-mesh copper TEM grid and dried for 1 h under an IR light. Powder X-ray diffraction (XRD) patterns were recorded on a Rigaku MiniFlex600 instrument equipped with a Cu Kα radiation (λ = 0.154178 nm) in the 2θ range of 10–80° with a step size of 0.01°. The lattice spacing d was calculated using Bragg's law: $2d \sin\theta$ =

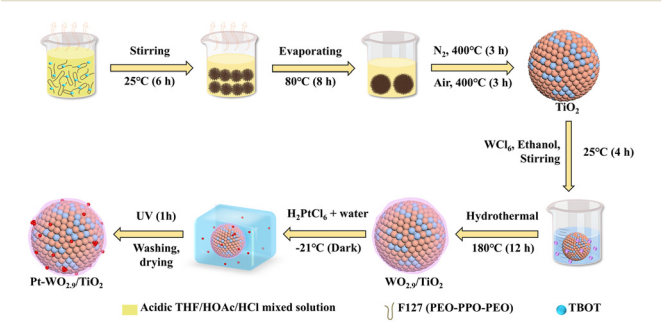

Scheme 1 Schematic of the synthesis of TiO_2 microspheres, $WO_{2.9}/TiO_2$, and Pt–$WO_{2.9}/TiO_2$ photocatalyst.

$n\lambda$. The Rietveld refinement line of TiO_2 was obtained using Maud software, in which the crystal structure models of anatase (9008213.cif) and rutile (9004141.cif) were introduced, respectively, and background and scale parameters, basic phase parameters, microstructure parameters, crystal structure parameters and all parameters for texture were adjusted in turn to calculate the ratio of rutile and anatase in TiO_2 microspheres. X-ray photoelectron spectroscopy (XPS) was performed on a Thermo Scientific K-Alpha instrument with a monochromatic Al Kα X-ray source (12 kV, 6 mA). The vacuum in the analysis room is 5.0 × 10^{-7} mbar. The binding energies of all the spectra were calibrated to the binding energy of C 1s at 284.6 eV.

2.4 Photocatalytic reduction of CO_2

The photocatalytic CO_2 reduction experiments were performed using a solid–vapor reaction in a Pyrex glass batch reactor with a window on top for light illumination (Labsolar 6A, Beijing Perfect light, China). The reaction temperature was controlled at approx. 10 °C by circulating cooling reagents at 5 °C. A 300 W Xe-lamp equipped with an AM 1.5 filter was placed on top and the optical power density was 100 mW cm^{-2}. 20 mg sample was dispersed in 1 mL of DI water and dipped on a porous ceramic substrate (Beijing Perfect Light Technology Co., Ltd) with a 30 mm diameter, then dried at 80 °C for 30 minutes. After drying, the substrate loaded with the catalyst was placed on the quartz support in the center of the reactor, 10 cm above the bottom of the reactor. The reactor was filled with 50 mL DI water at the bottom. After the reactor was sealed, it was continuously vacuum-treated for 10 minutes and purged three times with high-purity CO_2 (99.999%) gas, where CO_2 gas was bubbled through the water at the bottom of the reactor and continuously flowed until the pressure inside the reactor reached ~50 KPa. During irradiation, the products in the gas phase at different reaction times were analyzed by an online gas chromatograph (GC2030, SHIMADZU, Japan) with a barrier discharge ionization detector (BID) using high-purity helium (99.999%) as the carrier gas and Carboxen@1010 PLOT (30 m × 0.53 mm) as a chromatographic column. In blank experiments, in which there was no light source or photocatalyst, high-purity N_2 was used instead of CO_2.

The selectivity of CO_2 reduction (S_{CO_2}) and CH_4 (S_{CH_4}) are calculated using the following equations:

$$S_{CO_2} = \frac{8 \times \text{Yield}(CH_4) + 2 \times \text{Yield}(CO)}{8 \times \text{Yield}(CH_4) + 2 \times \text{Yield}(CO) + 2 \times \text{Yield}(H_2)}$$

$$S_{CH_4} = \frac{8 \times \text{Yield}(CH_4)}{8 \times \text{Yield}(CH_4) + 2 \times \text{Yield}(CO)}$$

2.5 Photoelectrochemical measurements

The photoelectrochemical measurements of TiO_2, Pt–TiO_2, $WO_{2.9}$/TiO_2, and Pt–$WO_{2.9}$/TiO_2 were performed in a three-electrode quartz electrolytic cell using an electrochemical workstation (Autolab PGSTAT 204A Instruments by Metrohm, Utrecht, Netherlands). The counter electrode was Ag/AgCl and the reference electrode was a platinum sheet (1 × 1 cm). The working electrode was prepared by the spin-coating method. 5 mg of the samples and 20 μL Nafion solution were placed into 0.5 mL of ethanol and sonicated for 1 h to obtain a uniform suspension, which was then uniformly coated on the glassy carbon electrode and dried in a vacuum oven at 80 °C. 0.5 M Na_2SO_4 solution was used as the electrolyte.

The transient photocurrent spectra were tested at a bias of 0.5 V with an on/off period of 40 s for each transient. The EIS measurements were carried out in the frequency range of 0.01–10^5 Hz at a bias of 0.5 V_{OCP}. Mott–Schottky (M–S) curves were obtained at frequencies of 600 Hz, 800 Hz, 1000 Hz and 1200 Hz in the potential range of −1.5–1.2 V.

2.6 DRIFTS measurements

DRIFTS measurements were conducted using a Thermo Scientific Nicolet FTIR spectrometer equipped with a liquid nitrogen-cooled HgCdTe (MCT) detector. The spectra were obtained by applying an average of 128 scans with a spectral resolution of 2 cm^{-1}. The final spectra were obtained after removing the background spectra.

DRIFTS for CO Adsorption. The chamber was purged with Ar (99.999%) at room temperature (RT) for 30 min to eliminate air after loading the samples and then the background spectrum was recorded. Subsequently, 8% CO in Ar was purged until the adsorption equilibrium was reached. The CO was then stopped by purging Ar into the chamber to remove the CO in the gas phase.

DRIFTS for *in situ* CO_2 reaction. The reaction chamber was purged with N_2 (99.999%) at 100 °C for 30 min to remove moisture and air from the sample and then cooled to RT. After recording the background spectrum in N_2, CO_2 (99.999%) and H_2O vapor *via* bubbling of CO_2 gas through water were introduced into the reaction chamber until adsorption equilibrium was reached. The chamber was then sealed and the spectra were recorded at certain time intervals under the illumination of a 300 W Xe lamp with an AM 1.5 filter.

2.7 DFT calculations

All the DFT calculations were performed using the Vienna *ab initio* simulation package (VASP)[22] with the projector augmented wave (PAW) method.[23] The exchange-functional is treated using the generalized gradient approximation (GGA) with Perdew–Burke–Ernzerhof (PBE)[24] functional. The energy cutoff for the plane-wave basis expansion was set to 450 eV. Partial occupancies of the Kohn–Sham orbitals were allowed using the Gaussian smearing method with a width of 0.2 eV. The $WO_{2.9}$ (010) and anatase TiO_2 (101) surfaces were constructed, where the Pt cluster with 10 Pt atoms was established loading on the surface. In addition, single atom Pt was constructed by replacing the W and Ti atoms on $WO_{2.9}$ (010) and anatase TiO_2 (101) surfaces, respectively. The

k-point of 2 × 1 × 1 and 1 × 1 × 1 was used for the calculations on $WO_{2.9}$ (010) and anatase TiO_2 (101) surfaces, respectively. The self-consistent calculations applied a convergence energy threshold of 10^{-5} eV, and the force convergency was set to 0.05 eV $Å^{-1}$.

The free energy corrections were calculated at 298 K using the following equation:

$$\Delta G = \Delta E + \Delta G_{ZPE} + \Delta G_U - T\Delta S$$

where ΔE, ΔG_{ZPE}, ΔG_U, and ΔS refer to the DFT-calculated energy change, the correction from zero-point energy, the correction from inner energy and the correction from entropy.[25]

3. Results and discussion

3.1 Morphology and structure analysis

In brief, TiO_2 microspheres were synthesized *via* solvent evaporation-driven oriented assembly using tetrabutyltitanate precursors.[12] A typical scanning electron microscopy (SEM) image of TiO_2 (Fig. 1a) exhibits a regular spheric shape with a diameter of 1.57 ± 0.10 μm, consisting of anatase (JCPDS 21-1272) and rutile (JCPDS 21-1276), with an R ($R = I_A/I_R$) of 23.6%, as determined by Rietveld refinement ((Fig. 1b, Table S1 and Fig. S1†). The homojunction between anatase and rutile in the microspheres allows for improved charge-carrier separation efficiency, higher reduction potential of electrons (E_{CB} of rutile ≤0.6 eV) and light absorption ability (E_g of rutile: ~3.0 eV).[26]

A substoichiometric tungsten oxide film was loaded onto TiO_2 microspheres *via* a hydrothermal method using tungsten hexachloride (WCl_6) as a metal precursor in deoxygenated anhydrous ethanol. The morphology of tungsten oxide depends on the concentration of WCl_6 in solution, but with TiO_2 microspheres as support, the morphology of tungsten oxide is directed by the support, where W^{6+} ions adsorb on the oxide sites, form nuclei and grow as a film (Fig. S2†).

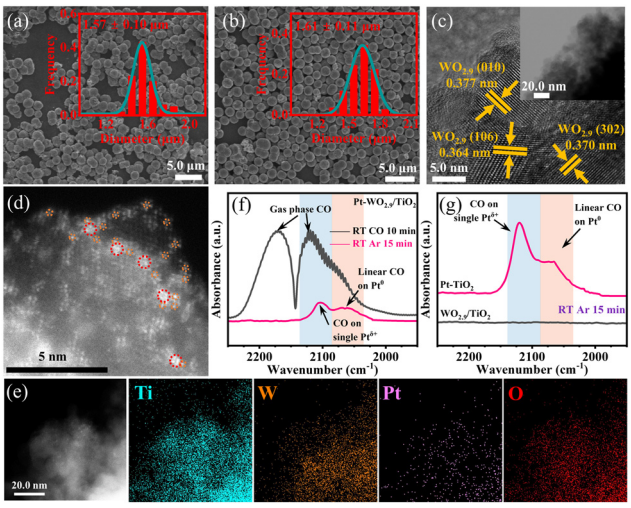

Fig. 1 SEM image and statistical analysis on particle size of (a) TiO_2 microspheres and (b) Pt–$WO_{2.9}$/TiO_2; (c) HRTEM image (inset: TEM image); (d) AC-HAADF-STEM image and (e) EDS elemental mapping of Pt–$WO_{2.9}$/TiO_2; CO-DRIFTS for (f) Pt–$WO_{2.9}$/TiO_2 and (g) Pt–TiO_2, $WO_{2.9}$/TiO_2.

The XRD spectrum (Fig. S1b†) for $WO_{2.9}$/TiO_2 shows no corresponding diffraction peaks for $WO_{2.9}$, which may be attributed to the high dispersion of $WO_{2.9}$ on the surface of TiO_2 microspheres. For reference, pure tungsten oxide in a dark blue color was synthesized using the same hydrothermal method. The XRD spectrum of the tungsten oxide (Fig. S3†) shows obvious diffraction peaks at 23.6° and 48.3°, which can be ascribed to the (010) and (020) facets in the $WO_{2.9}$ phase (JCPDS 05-0386). The Raman spectroscopy (Fig. S4†) revealed characteristic Raman active modes with symmetries E_g at 443 cm^{-1} and A_{1g} at 609 cm^{-1} for rutile TiO_2, and E_g at 144 cm^{-1} for anatase. The broad peak at about 230 cm^{-1} is aroused from the multiple phonons scattering. The attenuation of the peak at 144 cm^{-1} may be due to the change in the anatase phase in the TiO_2 microspheres. The coating amount of $WO_{2.9}$ was optimized based on the catalytic performance to be 10 wt% (Fig. S5a†).

The deposition of Pt was performed using photochemistry under restricted conditions.[27] The ice lattice naturally confines the dispersion of precursors, nucleus formation and crystal size. The density, size, dispersion and allocation of Pt atoms can be fine-regulated by the density of photoelectrons,[28] and the Pt precursor concentration. In this work, Pt cocatalysts were deposited as single atoms and nanoclusters on $WO_{2.9}$ film, reduced by photogenerated electrons under irradiation of ultraviolet light at λ = 275 nm. For reference, Pt cocatalysts were deposited on TiO_2 microspheres *via* the same photochemistry method and annotated as Pt–TiO_2. The amount of the Pt precursor was optimized based on the catalytic performance to be 1 wt% (Fig. S5b†).

The diameter of TiO_2 microspheres in Pt–$WO_{2.9}$/TiO_2 is 1.61 ± 0.11 μm, where the increase of 40 nm was attributed to the coating of $WO_{2.9}$ film (Fig. 1b). The lattice fringes at the edge of the microsphere were analyzed to be 0.377 nm, 0.370 nm and 0.364 nm from the HRTEM image (Fig. 1c and S6a†), corresponding to the (010), (302) and (106) crystal planes of $WO_{2.9}$, respectively.

The atomic dispersion of Pt was analyzed using aberration-corrected high-angle annular dark-field scanning TEM (AC HAADF-STEM) imaging (Fig. 1d and S6b†), which clearly resolves isolated Pt single atoms (marked by orange circles) and uniformly dispersed Pt clusters (marked by red circles) composed of several Pt atoms on $WO_{2.9}$, with no evidence of Pt nanoparticles exceeding 1 nm in size. The compositions of the elements were analyzed with a uniform distribution of Pt and W ((Fig. 1e). To further clarify the distribution of Pt, CO-adsorption diffuse reflectance infrared Fourier transform spectroscopy (CO-DRIFTS) measurements for Pt–$WO_{2.9}$/TiO_2 are performed (Fig. 1f). First CO coverage saturation is reached with two strong IR peaks for gas phase

CO. Then, gas phase CO and physically adsorbed CO were removed, which leaves chemical adsorption of CO with two sets of absorption bands centered at 2103 cm^{-1} and a broad peak at 2070 cm^{-1}. The former is ascribed to linearly adsorbed CO on single-atom $Pt^{\delta+}$,[29] and the latter is assigned to linearly adsorbed CO on Pt^0 in Pt particles.[30]

The CO-DRIFTS spectrum of $WO_{2.9}/TiO_2$ exhibits no clear bands for adsorbed CO (Fig. 1g), indicating that the CO adsorption bands observed for Pt–$WO_{2.9}/TiO_2$ originate from the CO adsorbed on the Pt species. For Pt–TiO_2, two sets of CO absorption bands are observed, with one centered at 2119 cm^{-1} and another broad band centered at 2070 cm^{-1}, where the former peak at 2119 cm^{-1} is attributed to CO adsorption on single $Pt^{\delta+}$ atoms. Compared with CO on Pt–$WO_{2.9}/TiO_2$ (2103 cm^{-1}), there is a blue shift in the CO adsorption peak on single $Pt^{\delta+}$ sites, indicating that the back donation from $WO_{2.9}$ to $Pt^{\delta+}$ is stronger than that from TiO_2. To evaluate the stability of Pt on TiO_2 and $WO_{2.9}/TiO_2$, the photocatalysts were pretreated in Ar/H_2 at 100 °C and CO-DRIFTS spectra were collected after the treatment (Fig. S7†).

X-ray photoelectron spectroscopy (XPS) was used to analyze the chemical species of the photocatalysts. The XPS survey spectra of TiO_2, Pt–TiO_2, $WO_{2.9}/TiO_2$ and Pt–$WO_{2.9}/TiO_2$ demonstrate that no impurity elements were present in the as-synthesized samples, except for Pt, W, O, Ti and C (Fig. S8†). The XPS Ti 2p spectrum of TiO_2 shows four symmetric peaks after deconvolution of the spectrum, with a pair of binding energy at 458.4 eV and 464.1 eV for Ti $2p_{3/2}$ and Ti $2p_{1/2}$ of Ti^{4+}, and another pair at 456.9 eV and 462.6 eV representing Ti $2p_{3/2}$ and Ti $2p_{1/2}$ for Ti^{3+}, with an area ratio of 36.5% for Ti^{3+} (Fig. 2a).

With the coating of $WO_{2.9}$, for the Ti 2p spectra of $WO_{2.9}/TiO_2$ and Pt–$WO_{2.9}/TiO_2$, a doublet peak at 458.4 eV for Ti $2p_{3/2}$ and 464.1 eV for Ti $2p_{1/2}$ of Ti^{4+} can be detected, where the shoulder peak of Ti^{3+} vanishes, which may be attributed to the oxidation during hydrothermal reaction in solution. During the formation of $WO_{2.9}$, electrons are preferentially extracted from Ti^{3+}-associated oxygen vacancies in TiO_2, thereby oxidizing Ti^{3+} to Ti^{4+}.

For Pt–TiO_2, the shoulder peak for Ti^{3+} vanished, possibly because of Pt deposition on the vacancy sites. However, the binding energy of Ti^{4+} shifts to lower energy (~0.30 eV), suggesting either the defects partially exist, or the electrons transfer from Pt to TiO_2 at the interface, which may induce upward surface band bending of TiO_2.

In the W 4f XPS spectrum of $WO_{2.9}/TiO_2$, two doublets can be deconvoluted-peaks with a binding energy of 35.2 eV and 37.3 eV attributed to W^{6+}, and another doublet at 33.9 eV and 36.0 eV attributed to W^{5+} (Fig. 2b). With Pt deposition, the peak of W^{6+} for Pt–$WO_{2.9}/TiO_2$ shifts to higher binding energy (~0.13 eV), indicating a decrease in the electron density of the W species, probably due to the transfer to the Pt sites. The shoulder peak for W^{5+} exists after the photodeposition of Pt, with an area ratio of 13.7%, which is close to the ratio for W^{5+} in $WO_{2.9}/TiO_2$ (13.0%) (Table S2†). Compared with the change in Ti 2p for Pt–TiO_2 after deposition of Pt, the defect sites in $WO_{2.9}$ remain for Pt–$WO_{2.9}/TiO_2$, suggesting a stable structure of substoichiometric $WO_{2.9}$.

The Pt $4d_{5/2}$ spectrum of Pt–$WO_{2.9}/TiO_2$ was resolved into three components, Pt^{4+} at 316.8 eV, Pt^{2+} at 314.4 eV, and Pt^0 at 311.6 eV (Fig. 2c). Compared with the Pt $4d_{5/2}$ spectrum for Pt–TiO_2, the binding energies of Pt^{2+} show a shift to lower binding energy (~0.20 eV, 314.6 eV), indicating an overall increase in the electron density of Pt on Pt–$WO_{2.9}/TiO_2$. For both samples, the Pt^{2+} species is dominant (~55%), but the concentration of Pt^0 species in Pt–TiO_2 (22.6%) is higher than that in Pt–$WO_{2.9}/TiO_2$ (15.7%) (Table S2†).

The O 1s XPS spectrum (Fig. 2d) of TiO_2 shows three components at 527.8 eV, 529.6 eV, and 531.7 eV, possibly corresponding to electron-rich oxygen (O_R < 529.0 eV), lattice O (O_L, Ti–O), and hydroxyl O (O_C, –OH), respectively.[31] With the coating of $WO_{2.9}$, for the O 1s spectra of $WO_{2.9}/TiO_2$ and Pt–$WO_{2.9}/TiO_2$, the peak related to electron-rich oxygen disappeared, which may be attributed to the oxidation during the hydrothermal reaction in solution. An additional peak at ~531.2 eV appears, which is characteristic of the oxygen-deficient tungsten oxide (O_V). Compared with the O 1s spectra for TiO_2 and $WO_{2.9}/TiO_2$, the O 1s spectra for Pt–TiO_2 and Pt–$WO_{2.9}/TiO_2$ show a shift to lower binding energy, which may be due to photoreduction and the interaction between the surface and deposited Pt.

The Mott–Schottky spectra show that the flat band (E_{fb}) potential of TiO_2 and $WO_{2.9}$ is −0.85 and 0.10 V *vs.* Ag/AgCl (about −0.65 and 0.30 V *vs.* NHE, E_{NHE} (V) = $E_{Ag/AgCl}$ + 0.197), respectively. (Fig. 3a) Furthermore, for n-type semiconductors, the conduction band minimum (CBM) is typically ~0.2 V more negative than the flat-band potential. Consequently, the CBM positions of TiO_2 and $WO_{2.9}$ were measured to be −0.85 V and 0.10 V (*vs.* NHE), respectively. The optical band gap was obtained from Tauc plots according to the following equation:

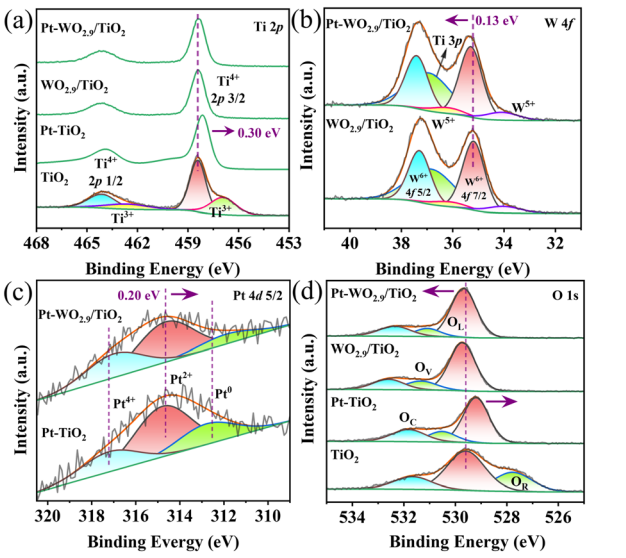

Fig. 2 High-resolution XPS spectra of (a) Ti 2p; (b) W 4f; (c) Pt 4d5/2; and (d) O 1s.

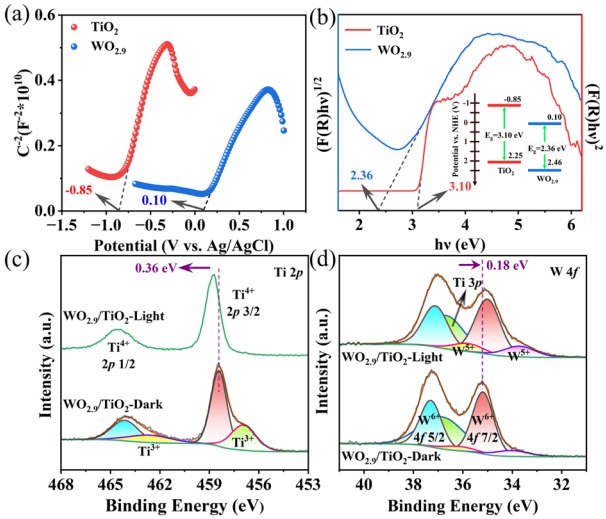

Fig. 3 (a) Mott–Schottky spectra and (b) Tauc plots of TiO_2 and $WO_{2.9}$, inset: proposed band structures of TiO_2 and $WO_{2.9}$. High-resolution XPS spectra of (c) Ti 2p, and (d) W 4f of $WO_{2.9}/TiO_2$ before and after light irradiation.

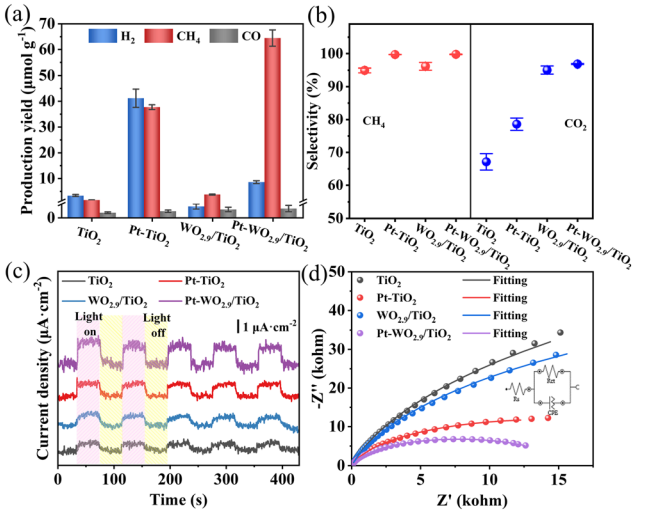

Fig. 4 Photocatalytic production yield (a) and selectivity (b) of TiO_2, $WO_{2.9}/TiO_2$, Pt–$WO_{2.9}/TiO_2$ and Pt–TiO_2 in a 6 h reaction time. (c) Photocurrent transient spectra and (d) electrochemical impedance spectra (EIS) of TiO_2, Pt–TiO_2, $WO_{2.9}/TiO_2$, and Pt–$WO_{2.9}/TiO_2$.

$$(\alpha h\nu)^n = A(h\nu - E_g)$$

where α is the absorption coefficient, h is Planck's constant and n is the vibration frequency (n = 2 for TiO_2, n = 1/2 for $WO_{2.9}$). The band gap (E_g) of TiO_2 and $WO_{2.9}$ was thus calculated to be 3.10 and 2.36 eV (ref. 32 and 33) (Fig. 3b), respectively. The band structures of TiO_2 and $WO_{2.9}$ are thus proposed to be a type II heterojunction.

In situ XPS Ti 2p and W 4f spectra under illumination (Fig. 3c and d) demonstrate that the Ti 2p peaks shifted +0.36 eV to higher binding energy, and the W 4f peaks shifted −0.18 eV, accompanied by an increase in W^{5+} content (13.7 → 24.0%). These observations confirm the directional electron transfer from TiO_2 to $WO_{2.9}$, consistent with a type II heterojunction mechanism.

3.2 Photocatalytic CO_2 reduction and photoelectrochemical performance

The above XPS analysis demonstrates the electronic interactions between $WO_{2.9}$ and Pt, and between $WO_{2.9}$ and TiO_2, which may contribute to the photocatalytic methane production. The photocatalytic CO_2 reduction performance of the Pt–$WO_{2.9}/TiO_2$ composites was evaluated and measured, leading to the production of CO, CH_4, and H_2 in the gas phase. Each experiment was repeated three times for the reference samples as TiO_2, Pt–TiO_2, and $WO_{2.9}/TiO_2$, to ensure reproducibility. The comparison of CH_4, H_2 and CO yield over reaction time under illumination is shown in Fig. S10.†

For TiO_2, the yield of CH_4 after 6 hours is 1.61 μmol g^{-1} (Fig. 4a), which increased to 3.68 μmol g^{-1} after coating with $WO_{2.9}$ for $WO_{2.9}/TiO_2$. For Pt–$WO_{2.9}/TiO_2$, the yield of CH_4 reaches 64.41 μmol g^{-1}, which is 17.5 times higher than that of $WO_{2.9}/TiO_2$. However, for Pt–TiO_2, the CH_4 yield is 37.63 μmol g^{-1}, which is about half of that for Pt–$WO_{2.9}/TiO_2$.

Compared with the methane production rate reported in the literature, the value reported in this work is among the top values (Table S4†). In the reference experiments, there was no detection of the gas product, *e.g.* CH_4 or CO, in the experiments without CO_2 (using substituted N_2), without light irradiation, or as a photocatalyst (Fig. S11†).

In addition, the H_2 yield is 3.34 μmol g^{-1} for TiO_2 and 0.80 μmol g^{-1} for $WO_{2.9}/TiO_2$, suggesting that the $WO_{2.9}/TiO_2$ heterojunction significantly improved the overall CO_2 conversion rate and suppressed the competing reaction for hydrogen evolution. Moreover, the hydrogen yield is 41.12 μmol g^{-1} for Pt–TiO_2, which is 4.8 times higher than that for Pt–$WO_{2.9}/TiO_2$ (8.47 μmol g^{-1}), indicating that the deposition of Pt promotes the hydrogen evolution reaction, but with $WO_{2.9}$, hydrogen evolution can be effectively inhibited.

The selectivity of CO_2 reduction (S_{CO_2}) and CH_4 (S_{CH_4}) are calculated based on the yield, where S_{CO_2} refers to the selectivity for electron consumption CO_2 reduction (see Fig. S12†) in competition with hydrogen evolution, and S_{CH_4} refers to the methane selectivity among CH_4 and CO (Fig. 4b). The S_{CO_2} is 67.1% for TiO_2 microspheres, which increases significantly to 95.0% with the loading of $WO_{2.9}$ and reaches a remarkably high value of 96.8% for Pt–$WO_{2.9}/TiO_2$. However, S_{CO_2} for Pt–TiO_2 decreases to 78.6%, which suggests that the presence of $WO_{2.9}$ facilitates the electron transfer to CO_2 reduction reaction.

The stability of Pt–$WO_{2.9}/TiO_2$ was evaluated by performing six consecutive reaction cycles (6 hours for each). The average methane production rate in the fifth cycle was 73.3% of the first cycle (Fig. S13†), showing a slight decrease in the activity, which may stem from partial deactivation of the Pt active sites or surface contamination by intermediates.

To understand the impact of Pt sites on the CO_2 reduction reaction, Pt NP–$WO_{2.9}$/TiO_2 was prepared by annealing Pt–$WO_{2.9}$/TiO_2 in N_2 to convert Pt to nanoparticles. The methane production rate of Pt NP–$WO_{2.9}$/TiO_2 significantly decreased to 5.25 μmol g^{-1} h^{-1}, and the hydrogen production rate increased to 19.19 μmol g^{-1} h^{-1} (Fig. S14†), that gives a S_{CO_2} of 52.4%. These results indicate that the competitive reaction of hydrogen evolution is favoured on Pt nanoparticles.

The S_{CH_4} among CH_4 and CO for TiO_2 was 94.9%, that is like S_{CH_4} for $WO_{2.9}$/TiO_2 (96.2%). In the presence of Pt, the S_{CH_4} is 99.8% for Pt–$WO_{2.9}$/TiO_2, 99.7% for Pt–TiO_2, and 99.9% for Pt NP–$WO_{2.9}$/TiO_2, which suggests that Pt can significantly improve the methane selectivity, possibly contributing to the proton production and spillover during the reaction.

The photocurrent density of Pt–$WO_{2.9}$/TiO_2 (1.77 μA cm^{-2}) is nearly 3 times as compared to TiO_2 (0.56 μA cm^{-2}), demonstrating a significant improvement in the separation and transfer of photogenerated charge carriers (Fig. 4c). The electrochemical impedance spectroscopy (EIS) spectra show that the charge transfer resistance of Pt–$WO_{2.9}$/TiO_2 is 15.31 kOhm, which is lower than the R_{ct} of Pt–TiO_2 (27.92 kOhm, Table S5†). The lower charge transfer resistance favoured the transport and separation of photogenerated electron–hole pairs (Fig. 4d). The coating of $WO_{2.9}$ on TiO_2 not only extends the absorption edge but improves the separation efficiency of photogenerated carriers.

After five cycles of experiments, the post-reaction photocatalyst was analysed. A slight decrease in photocurrent density (Fig. S15a†) and an increase in charge transfer resistance (Fig. S15b†) are in line with a decrease in photocatalytic activity, possibly due to partial deactivation of the Pt active sites.

3.3 CO_2 photoreduction mechanism

Except for the charge transfer kinetics, the surface reaction rate also determines the overall reaction rate. The reaction intermediates during the photocatalytic methane production were thus detected by *in situ* DRIFTS measurements (Fig. 5 and S16†). After the adsorption equilibrium of CO_2 and water vapor, the DRIFTS for Pt–$WO_{2.9}$/TiO_2 (Fig. 5a, bottom spectrum) show the peaks at 1273 cm^{-1}, 1372 cm^{-1}, 1424 cm^{-1}, 1700 cm^{-1}, that could be attributed to the features of the *COOH intermediates, that is, OH deformation, C–O stretch, symmetric stretch and C═O stretch, respectively. The signals appeared at 1067 cm^{-1}, 1464 cm^{-1}, 1150 cm^{-1} can be assigned to *CHO, *CH_2O and *OCH_3, respectively. Furthermore, the *CO absorption band at ~2077 cm^{-1} can be detected, indicating abundant CO intermediates were generated on the surfaces after the adsorption of CO_2 and the *CHO intermediate originated from *CO. The bands at 2987 cm^{-1} to 2898 cm^{-1} can be attributed to the –CH_3/–CH_2 stretch and the wide band at 1637 cm^{-1} can also be observed, which is attributed to physically adsorbed H_2O. The results suggest that the dissociation of CO_2, H_2O and proton reactions occur on the surface after the adsorption of CO_2 and H_2O in the dark.

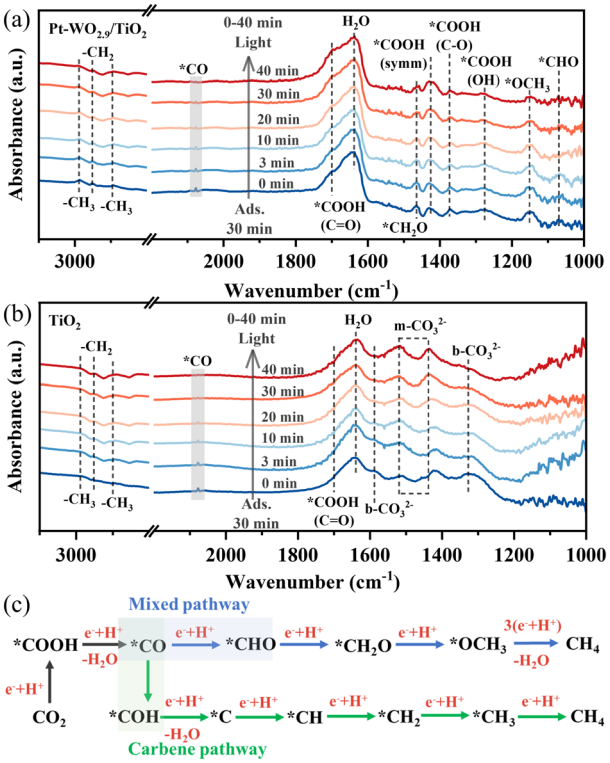

Fig. 5 *In situ* DRIFTS spectra recorded during the photocatalytic CO_2 reduction of (a) Pt–$WO_{2.9}$/TiO_2 and (b) TiO_2. (c) Proposed pathways for CO_2 methanation.

After illumination of the Xe lamp with AM 1.5 filter, the DRIFTS feature for *CO at ~2077 cm^{-1} and the bands at 2987 to 2898 cm^{-1} for –CH_3/–CH_2 stretching almost vanishes, suggesting that the intermediates were consumed during the reaction. The intensity for the *CHO at 1067 cm^{-1}, *OCH_3 at 1150 cm^{-1} and *CH_2O at 1464 cm^{-1} decrease during the 40 min illumination duration. However, the intensity of the signals for the *COOH intermediate features increased over the illumination time, that is OH deformation at 1273 cm^{-1}, symmetric stretch at 1424 cm^{-1}, and C═O stretch at 1700 cm^{-1}. Based on the above analysis, the pathway of CO_2 methanation on Pt–$WO_{2.9}$/TiO_2 photocatalyst is a mixed pathway (Fig. 5c).

For the DRIFTS of TiO_2 (Fig. 5b), after the adsorption of CO_2, the peaks of monodentate carbonates at 1518 cm^{-1} and 1437 cm^{-1} (m-CO_3^{2-}), bidentate carbonates at 1587 cm^{-1}, and 1327 cm^{-1} (b-CO_3^{2-}) can be detected, as well as *CO at 2077 cm^{-1}, physically adsorbed H_2O at 1638 cm^{-1} and –CH_3/–CH_2 at 2987 to 2898 cm^{-1}. After illumination of AM1.5 for 40 min, the signal of the IR peaks related to b-CO_3^{2-} and *CO intermediates completely vanishes, but the intensity for the bands at 1518 and 1437 cm^{-1} for m-CO_3^{2-} increases over illumination time. Moreover, the intensity of the characteristic peak at 1700 cm^{-1} of *COOH (C═O) hardly changes with illumination. The above phenomena indicate

that light excitation enhances the adsorption and activation ability of TiO_2 for CO_2 gas (CO_2 to adsorbed carbonate species), but the protonation process of the intermediates is limited, resulting in low catalytic efficiency. In addition, CO_2 methanation on TiO_2 occurs *via* the carbene pathway. The formation of the *CO intermediate needs to overcome a high energy barrier to form the *C intermediate, so CH_4 production through the mixed pathway is favoured instead of the carbene pathway.[34] Hence, the CH_4 yield and selectivity of Pt–$WO_{2.9}$/TiO_2 are higher than those of TiO_2, consistent with the yield and reaction rate detected in the CO_2 photoreduction experiments.

The DRIFTS spectra of Pt–TiO_2 and $WO_{2.9}$/TiO_2 were acquired as a reference (Fig. S16†). Compared to TiO_2, the peaks of b-CO_3^{2-} disappear and the intensity of peaks related to m-CO_3^{2-} significantly decreased in the DRIFTS spectra of $WO_{2.9}$/TiO_2 acquired after adsorption and under illumination, and the intensity of the peak related to *COOH (C═O) significantly increased with the extension of illumination time (Fig. S16a†). The *COOH species is a key intermediate in the photoreduction of CO_2 to CO or CH_4, and its formation and adsorption behavior significantly affect the yield and selectivity of the CO_2 reduction reaction relative to the hydrogen evolution reaction.

For the DRIFTS of Pt–TiO_2 in the dark and under illumination (Fig. S16b†), the intensity of the peaks related to *COOH (C═O) also increased. The peak corresponding to *CH_3O at 1150 cm^{-1} appears after adsorption of CO_2 and the intensity decreased over time under illumination, demonstrating that the Pt sites regulate the CO_2 methanation pathway from carbene to mixed pathway.

Based on the above discussion and analysis, it is clear that the most significant adsorption peak of the *COOH species appears for Pt–$WO_{2.9}$/TiO_2, but no observation of the adsorption peak corresponding to the carbonate species before and after illumination suggests that the synergy between $WO_{2.9}$ and Pt sites can promote the conversion of CO_2 into the *COOH intermediate. The absence of carbonate intermediates indicates that the reaction followed a proton-induced pathway for CO_2 reduction (CO_2 → $COOH^+$ → *COOH).

In addition to the photoelectric performance and spectroscopic analysis, it can be determined that the formation of $WO_{2.9}$/TiO_2 heterojunction and the loading of Pt sites on the $WO_{2.9}$ film significantly improve the light absorption and achieve a higher separation efficiency of photogenerated carriers. Furthermore, the strong Lewis acidity of the $WO_{2.9}$ film, the electron-rich nature of the Pt sites and the hydrogen spillover channel from Pt clusters (Pt NPs) to Pt single atoms (Pt_1) optimize the adsorption and activation processes of CO_2, significantly promoting the generation of key intermediates for CO_2 methanation, such as *COOH and *OCH_3. Consequently, the highest CH_4 production and selectivity in Pt–$WO_{2.9}$/TiO_2 are simultaneously achieved.

Hydrogen spillover occurs between noble metal particles and oxide supports (particularly reducible support), which

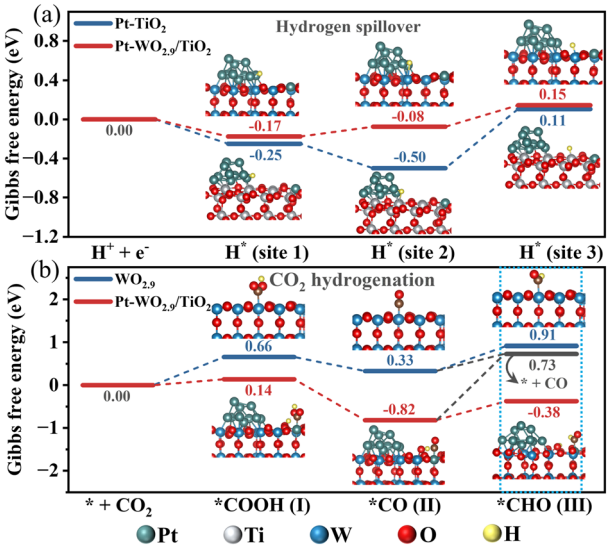

Fig. 6 Calculated free energy diagram for (a) hydrogen spillover on Pt/$WO_{2.9}$ in comparison to Pt/TiO_2 and (b) CO_2 to *CHO or CO on Pt_1/$WO_{2.9}$/TiO_2 and on $WO_{2.9}$. The insets are stick-ball models, showing the stable adsorption configuration of intermediates on the active sites.

allows the migration of active hydrogen atoms from metal particles (where a hydrogen atom is generated) to the support.[35,36] In the hydrogen evolution reaction, the hydrogen spillover effect can significantly enhance reaction rates.[37–39] Therefore, the rational design of spillover pathways on the catalyst can effectively improve CO_2 hydrogenation rates by suppressing competitive HER.[16,40]

To further evaluate the hydrogen spillover assisted by $WO_{2.9}$, density functional theory (DFT) calculations were performed using Pt/TiO_2 and Pt–$WO_{2.9}$/TiO_2. Fig. 6a shows that on the Pt–$WO_{2.9}$ surface, H* preferentially absorbs at the Pt/$WO_{2.9}$ interface with ΔG_H values of −0.17 eV (site 1) and −0.08 eV (site 2), where the negative values indicate spontaneous hydrogen adsorption. The ΔG_H at the W top site (site 3, between Pt NPs and Pt_1) was 0.15 eV, resulting in a thermodynamic energy barrier from site 2 to site 3 of 0.23 eV. On the surface of Pt–TiO_2, the values of ΔG_H on site 1 and site 2 were −0.25 eV and −0.50 eV, respectively, indicating spontaneous hydrogen bonding at the interface between the Pt cluster and TiO_2. The ΔG_H for H* adsorption on the Ti top (site 3) was 0.11 eV, leading to a considerably higher thermodynamic energy barrier (0.61 eV) from site 2 to site 3, compared to the Pt–$WO_{2.9}$/TiO_2, which may hinder hydrogen spillover from site 2 to site 3 on the surface of TiO_2.

Based on the results of CO_2 photoreduction experiments, the highest H_2 production rate (19.19 μmol g^{-1} h^{-1}) is observed for Pt NPs on $WO_{2.9}$/TiO_2 without Pt_1, suggesting that protons may accumulate on Pt NPs and recombine to form hydrogen gas, which is a competitive reaction process for methane production. With Pt_1 and Pt clusters (Pt–$WO_{2.9}$/TiO_2), H_2 production rate decreased significantly (1.42 μmol g^{-1} h^{-1}), and the methane production rate greatly increased (10.74 μmol g^{-1} h^{-1}). In addition, for 2Pt–$WO_{2.9}$/TiO_2 (with nominal 2.0 wt% Pt precursor), the hydrogen evolution rate

was nearly two times higher than that of Pt–$WO_{2.9}$/TiO_2 (Fig. S5b†). Therefore, Pt SAs optimize CO_2 adsorption/activation, and Pt clusters enhance H_2O dissociation, which synergistically determines the overall activity and selectivity for CO_2 methanation.

For the sample without $WO_{2.9}$ (Pt–TiO_2), the methane production rate is 6.27 μmol g^{-1} h^{-1} and the H_2 production rate is 6.85 μmol g^{-1} h^{-1}, which may be due to the limited spillover of hydrogen. The experimental results and DFT calculations demonstrate that during the photocatalytic reduction reaction, protons at the Pt clusters transfer from the interface between the Pt clusters and the oxide support to the surface of the oxide, then desorb and participate in the reaction with CO_2 molecules on adjacent Pt_1, where the spillover is favoured on the $WO_{2.9}$, in comparison to TiO_2. The synergistic effect of Pt clusters and Pt_1 and the promotion of $WO_{2.9}$ on hydrogen spillover led to high efficiency for CO_2 methanation and inhibited HER activity.

To further demonstrate the role of the synergistic Pt sites, calculations on the Gibbs free energy pathways of CO_2 reduction from adsorbed CO_2 to *CHO or CO were performed using Pt–$WO_{2.9}$/TiO_2 and bare $WO_{2.9}$ (Fig. 6b). On the surface of bare $WO_{2.9}$, ΔG_H value of CO_2 to *COOH was 0.66 eV, which decreased to 0.14 eV for Pt–$WO_{2.9}$/TiO_2. The lower energy barrier on the surface of Pt–$WO_{2.9}$/TiO_2 can be ascribed to the electronic structure of Pt_1 favouring the adsorption compared to that of W. Moreover, due to the hydrogen spillover to the O atom adjacent to Pt_1, an OH bond forms near Pt_1, which can significantly weaken the original Pt–O bond (Fig. S17†). Consequently, when a C_1 intermediate adsorbs and forms a chemical bond with Pt_1, the Pt–O bond strengths further decrease and may break, leading to stable adsorption of the C1 intermediate on the Pt_1 site (inset in Fig. 6b).

In addition, on Pt–$WO_{2.9}$/TiO_2, the energy barrier from *CO to *CHO was 0.44 eV, which was significantly lower than the energy barrier for *CO desorption (1.55 eV). Therefore, *CO tends to further protonation reaction rather than desorption of CO on Pt–$WO_{2.9}$/TiO_2. However, in $WO_{2.9}$, the energy barrier from *CO to desorbed CO molecules was 0.40 eV, which was lower than the energy barrier from *CO to *CHO (0.58 eV). Therefore, *CO intermediates tend to desorb from the $WO_{2.9}$ surface to free CO molecules, which is in line with the experimental results, in which the CO production rate is higher for $WO_{2.9}$/TiO_2 without Pt presence on the surface.

For Pt–$WO_{2.9}$/TiO_2, CH_4 selectivity reaches almost 100% with highest production rate under simulated solar light. Hydrogen spillover from Pt clusters to the vicinity of Pt_1 sites not only regulates the coordination environment of Pt_1 sites for CO_2 adsorption and activation but also provides protons for CO_2 methanation.

4. Conclusion

In this work, CO_2 molecules were converted to methane using a Pt–$WO_{2.9}$/TiO_2 photocatalyst, achieving a high CH_4 selectivity of 99.8% and an average CH_4 production rate of 10.74 μmol g^{-1} h^{-1} under simulated solar light. Dissociated water on the Pt clusters provides active H* for CO_2 methanation through the hydrogen spillover channel, while the Pt single atoms act as the adsorption and activation sites for CO_2. The strong Lewis acidity of $WO_{2.9}$ enhances hydrogen spillover, effectively inhibiting the competitive hydrogen evolution activity. Moreover, the hydrogen spillover influences the coordination of Pt_1 for the adsorption of C_1 intermediates and reduces the energy barrier for further protonation. The yield of CH_4 is thus enhanced by promoting the activation of CO_2 molecules and the CH_4 production pathways. Therefore, this work provides insights into the atomic design of cost-effective photocatalysts for CO_2 methanation.

Data availability

The data supporting this article have been included as part of the ESI.†

Conflicts of interest

There are no conflicts to declare.

Acknowledgements

This work was financially supported by the National Natural Science Foundation of China (No. 22108179, X. Z., 22308234, C. Z., 22176135 C. L.) and the Postdoctoral Fellowship Program of CPSF (GZC20231775, C. Z.). The authors would like to thank Dr. Yingming Zhu at the Institute of New Energy and Low-Carbon Technology for UV-vis measurements, and Yanping Huang at the Center of Engineering Experimental Teaching, School of Chemical Engineering, Sichuan University.

References

1 X. Meng, X. Cui, N. P. Rajan, L. Yu, D. Deng and X. Bao, *Chem*, 2019, **5**, 2296–2325.
2 M. Tommasi, S. N. Degerli, G. Ramis and I. Rossetti, *Chem. Eng. Res. Des.*, 2024, **201**, 457–482.
3 U. Ulmer, T. Dingle, P. N. Duchesne, R. H. Morris, A. Tavasoli, T. Wood and G. A. Ozin, *Nat. Commun.*, 2019, **10**, 3169.
4 T. Zhang, X. Han, N. T. Nguyen, L. Yang and X. Zhou, *Chin. J. Catal.*, 2022, **43**, 2500–2529.
5 X. Li, J. Yu, M. Jaroniec and X. Chen, *Chem. Rev.*, 2019, **119**, 3962–4179.
6 J. Fu, K. Jiang, X. Qiu, J. Yu and M. Liu, *Mater. Today*, 2020, **32**, 222–243.
7 T. Paik, M. Cargnello, T. R. Gordon, S. Zhang, H. Yun, J. D. Lee, H. Y. Woo, S. J. Oh, C. R. Kagan, P. Fornasiero and C. B. Murray, *ACS Energy Lett.*, 2018, **3**, 1904–1910.
8 K. Manthiram and A. P. Alivisatos, *J. Am. Chem. Soc.*, 2012, **134**, 3995–3998.

9 H. Khan, M. G. Rigamonti and D. C. Boffito, *Appl. Catal., B*, 2019, **252**, 77–85.
10 C. Lu, J. Li, J. Yan, B. Li, B. Huang and Z. Lou, *Appl. Mater. Today.*, 2020, **20**, 100744.
11 F. Riboni, L. G. Bettini, D. W. Bahnemann and E. Selli, *Catal. Today*, 2013, **209**, 28–34.
12 Y. Liu, R. Che, G. Chen, J. Fan, Z. Sun, Z. Wu, M. Wang, B. Li, J. Wei, Y. Wei, G. Wang, G. Guan, A. A. Elzatahry, A. A. Bagabas, A. M. Al-Enizi, Y. Deng, H. Peng and D. Zhao, *Sci. Adv.*, 2015, **1**, e1500166.
13 L. Yang, J. Du, J. Deng, N. H. M. Sulaiman, X. Feng, C. Liu and X. Zhou, *Small*, 2024, **20**, 2307007.
14 J. Ran, M. Jaroniec and S.-Z. Qiao, *Adv. Mater.*, 2018, **30**, 1704649.
15 C. Dong, C. Lian, S. Hu, Z. Deng, J. Gong, M. Li, H. Liu, M. Xing and J. Zhang, *Nat. Commun.*, 2018, **9**, 1252.
16 Y. Wang, J. Zhao, Y. Li and C. Wang, *Appl. Catal., B*, 2018, **226**, 544–553.
17 S. Xie, Y. Wang, Q. Zhang, W. Deng and Y. Wang, *ACS Catal.*, 2014, **4**, 3644–3653.
18 H. Wang, L. Zhang, Y. Zhou, S. Qiao, X. Liu and W. Wang, *Appl. Catal., B*, 2020, **263**, 118331.
19 X. Shi, Y. Huang, Y. Bo, D. Duan, Z. Wang, J. Cao, G. Zhu, W. Ho, L. Wang, T. Huang and Y. Xiong, *Angew. Chem., Int. Ed.*, 2022, **61**, e202203063.
20 L. Kuai, Z. Chen, S. Liu, E. Kan, N. Yu, Y. Ren, C. Fang, X. Li, Y. Li and B. Geng, *Nat. Commun.*, 2020, **11**, 48.
21 S. Yin, Y. Zhou, Z. Liu, H. Wang, X. Zhao, Z. Zhu, Y. Yan and P. Huo, *Nat. Commun.*, 2024, **15**, 437.
22 G. Kresse and J. Furthmüller, *Comput. Mater. Sci.*, 1996, **6**, 15–50.
23 P. E. Blöchl, *Phys. Rev. B: Condens. Matter Mater. Phys.*, 1994, **50**, 17953–17979.
24 J. P. Perdew, J. A. Chevary, S. H. Vosko, K. A. Jackson, M. R. Pederson, D. J. Singh and C. Fiolhais, *Phys. Rev. B: Condens. Matter Mater. Phys.*, 1992, **46**, 6671–6687.
25 C. Guo, X. Tian, X. Fu, G. Qin, J. Long, H. Li, H. Jing, Y. Zhou and J. Xiao, *ACS Catal.*, 2022, **12**, 6781–6793.
26 C. Gao, T. Wei, Y. Zhang, X. Song, Y. Huan, H. Liu, M. Zhao, J. Yu and X. Chen, *Adv. Mater.*, 2019, **31**, 1806596.
27 H. Wei, K. Huang, D. Wang, R. Zhang, B. Ge, J. Ma, B. Wen, S. Zhang, Q. Li, M. Lei, C. Zhang, J. Irawan, L.-M. Liu and H. Wu, *Nat. Commun.*, 2017, **8**, 1490.
28 A. Kubiak, *Sci. Rep.*, 2024, **14**, 13827.
29 W. Zhang, H. Wang, J. Jiang, Z. Sui, Y. Zhu, D. Chen and X. Zhou, *ACS Catal.*, 2020, **10**, 12932–12942.
30 K. Ding, A. Gulec, A. M. Johnson, N. M. Schweitzer, G. D. Stucky, L. D. Marks and P. C. Stair, *Science*, 2015, **350**, 189–192.
31 M. Kan, C. Yang, Q. Wang, Q. Zhang, Y. Yan, K. Liu, A. Guan and G. Zheng, *Adv. Energy Mater.*, 2022, **12**, 2201134.
32 L. Li, X. Dai, C. Cheng, F. Chen, S. M. Wabaidur, W. Wang and Y. Hu, *Chem. Eng. J.*, 2025, **507**, 160101.
33 L. Li, H. Liu, C. Cheng, X. Dai, F. Chen, J. Ning, W. Wang and Y. Hu, *ACS Catal.*, 2024, **14**, 10204–10213.
34 Ș. Neațu, J. A. Maciá-Agulló, P. Concepción and H. Garcia, *J. Am. Chem. Soc.*, 2014, **136**, 15969–15976.
35 W. C. Conner, Jr. and J. L. Falconer, *Chem. Rev.*, 1995, **95**, 759–788.
36 M. D. Marcinkowski, A. D. Jewell, M. Stamatakis, M. B. Boucher, E. A. Lewis, C. J. Murphy, G. Kyriakou and E. C. H. Sykes, *Nat. Mater.*, 2013, **12**, 523–528.
37 Z. Gu, M. Li, C. Chen, X. Zhang, C. Luo, Y. Yin, R. Su, S. Zhang, Y. Shen, Y. Fu, W. Zhang and F. Huo, *Nat. Commun.*, 2023, **14**, 5836.
38 J. Li, J. Hu, M. Zhang, W. Gou, S. Zhang, Z. Chen, Y. Qu and Y. Ma, *Nat. Commun.*, 2021, **12**, 3502.
39 J. Li, H.-X. Liu, W. Gou, M. Zhang, Z. Xia, S. Zhang, C.-R. Chang, Y. Ma and Y. Qu, *Energy Environ. Sci.*, 2019, **12**, 2298–2304.
40 P. Liu, Z. Huang, X. Gao, X. Hong, J. Zhu, G. Wang, Y. Wu, J. Zeng and X. Zheng, *Adv. Mater.*, 2022, **34**, 2200057.